



Experimental Study of Development of Fracture Process Zone in Rock

Yang Qiao · Zong-Xian Zhang · Sheng Zhang

Received: 5 December 2021 / Accepted: 19 April 2023 / Published online: 29 September 2023
© The Author(s) 2023

Abstract By means of digital image correlation (DIC) technology, the displacements and strains on the fracture ligaments of rock specimens were measured during loading. By analyzing the displacement distribution of each fracture ligament at different loading stages, the displacement fluctuation coefficient method was proposed to describe the development of fracture process zone (FPZ). The method can amplify the variation of displacement and clearly show the length of FPZ. The results show that: (1) the initiation of FPZ occurred at 77–89% of the peak load and the fluctuation coefficient of horizontal displacement around the crack tip reached the order of 10^{-7} . (2) The initial length of FPZ was about 1.0–3.1 mm, which is 2 to 6 times the largest grain sizes. As the peak load was approached, the length of FPZ suddenly increased to 4.6–6.1 mm. (3) When a fracture process zone was initiated, the strain at the front end of the FPZ was about 3000–4000 $\mu\epsilon$. After the load approached the peak value, the strain at the rear end of the FPZ finally reached a peak value of 8000–11000 $\mu\epsilon$ in all specimens.

Keywords Fracture process zone · Fluctuation coefficient · Initiation · Development

Abbreviations

CNB	Center notch beam
CZM	Cohesive zone model
DIC	Digital image correlation technology
FPZ	Fracture process zone

List of symbols

u	Horizontal displacement
v	Vertical displacement
w	Middle deflection of the beam
λ	Fluctuation coefficient

1 Introduction

Fracture process zone (FPZ) is an irreversible deformation and damage zone in the front of a crack tip in rock, where the constitutive stress–strain relationship is nonlinear. This nonlinear zone was first proposed in metallic materials by Orowan to resolve the contradiction between critical energy release rate G_c and surface energy γ_s in Griffith theory (Orowan 1949). Dugdale (1960) and Barenblatt (1962) developed a model to describe the internal development mechanism of a damage zone near a crack tip. This model was called D-B model (or cohesive zone model) which explained that the damage zone was a region with cohesion,

Y. Qiao (✉) · Z.-X. Zhang
Oulu Mining School, University of Oulu, Oulu, Finland
e-mail: Yang.Qiao@oulu.fi

S. Zhang
School of Energy Science and Engineering, Henan
Polytechnic University, Jiaozuo, China

and traction force acted on the microscopically separated surfaces surrounding the crack tip. Inspired by the D-B model, Hillerborg et al. (1976) proposed the fictitious crack model (FCM) and introduced the concept of fracture process zone for concrete. For rocks, FPZ was defined as a non-linear region and it was characterized by micro-cracking around the crack tip and interlocking along a portion of mineral grains (Labuz et al. 1985; Brooks et al. 2013).

Maji and Wang (1992) found that grain size was an important factor affecting the formation and size of FPZ, and “crack bridging” phenomenon was the main feature of FPZ formation. According to fracture experiments (Kaminsky et al. 2004a,b), “crack bridging” phenomenon indicated that the tip of (main) crack, although microcracks existed in the region, could continue to resist the propagation of the crack due to the contact friction of mineral grains, aggregate interlock, unbroken fiber, and so on. By scanning the distribution of mineral grains and micro-damages in the fracture ligament of loaded specimens, Ghamgosar and Erarslan (2016) found that mineral grains would be deboned and loosen as the FPZ developed under cyclic loading. They confirmed that the “crack bridging” phenomenon was the main feature of the FPZ formation. Besides, the displacement in the FPZ was discontinuous (Wu et al. 2020; Zhang et al. 2021a, b).

According to the deformation characteristics and mechanical properties of FPZ, there are two ways to determine FPZ sizes: experiment method and theoretical analysis. In terms of theoretical analysis, Ouchterlony (1982), Schmidt (1980), Schmidt and Lutz (1979) determined the shape of FPZ using the maximum principal stress criterion based on previous experiments. Whittaker et al. (1992) further gave the calculation formula. Then the theory of critical distances was developed to calculate the length of FPZ (Justo et al. 2017). In the theory, the length of FPZ can be calculated by using the fracture toughness and tensile strength of rock. Another theory, the cohesive zone model mentioned earlier, correlated the cohesive forces and the tensional displacements within the FPZ and it was found to be an effective tool for analysing FPZ (Dong et al. 2019; Garg et al. 2021).

In the experimental study, Fakhimi and Tarokh (2013, 2017), Fakhimi et al. (2017) determined the length and width of FPZ by acoustic emission (Tarokh et al. 2017), and the length and width of FPZ were found to increase with increasing specimen size.

Lin and Labuz (2013), Lin et al. (2014) obtained the full-field displacement of rock specimens by the DIC, determined the length of FPZ according to the deformation characteristics in the FPZ, and measured the length of FPZ under the Model I and II. Using computation tomography (CT), Willett et al. (2017) examined the three-dimensional image of FPZ by dip-coating the three-point bending beam with barium sulfate solution, and measured the sizes of FPZ. Qiao and Zhang (2020) determined the sizes of FPZ by the displacement fluctuation coefficient method. Zhang et al. (2021a, b) identify the length and width of the FPZ according to the variations of the displacement field at the crack tip.

On the basis of the experimental studies on the sizes of FPZ, many researchers investigated the size development and evolution of FPZ. For example, Vavro et al. (2017) used X-ray technology to observe the overall shape and evolution of FPZ during loading. Regrettably, Vavro did not quantitatively analyze the size variation of FPZ. According to the deformation and mechanical properties of FPZ, Veselý and Frantík (2014) designed a program to calculate the range of FPZ in different loading periods. Their results showed that the shape of FPZ was approximately elliptical. Zhang et al. (2021a, b) found that the FPZ begins to develop as the load reaches around 65% pre-peak. The range of the FPZ reaches the maximum at the peak load. The closer to the peak load, the faster the development of the FPZ. A large number of experiments with scanning electronic microscope (SEM) revealed that microcracks and branching cracks appeared at or near the tip of a main crack in rock fracture under dynamic loads (Bieniawski 1968; Zhang et al. 2000, 2001) and layer cracks occurred close to the fracture surfaces of a main crack under quasi-static loading (Zhang et al. 2000).

Many previous studies have investigated the deformation characteristics and size determination of FPZ, but only a few of them experimentally focused the size development of FPZ during loading process. Some previous studies have shown that: (1) FPZ development is one of main reasons for creep damage in rocks (Evans and Fuller 1974; Ghamgosar and Erarslan 2016). (2) The study about the development of FPZ can construct suitable cohesive law (strain softening law) which is necessary in cohesive zone model and relevant numerical simulations (Rice 1964; Turon et al. 2007). (3) FPZ development leads to size effects of fracture toughness (Bazant 1976; Hu

and Duan 2008). (4) The true energy release rate G can be estimated by studying the energy consumed during FPZ development, since FPZ contains a large number of micro-cracks that consume considerable elastic energy (Friedman et al. 1972; Labuz et al. 1987; Zhang and Ouchterlony 2022). In brief, it is necessary to investigate the development of FPZ by experimental methods.

In this study, the DIC was used to monitor the initiation and development of FPZ in three-point bending rock beams during loading, and the length of FPZ was determined by the fluctuation coefficient method. The variation of displacement and strain in FPZ was included and revealed during loading.

2 Experimental Methods

2.1 Digital Image Correlation (DIC) Technology

The DIC technology, based on photometric mechanics and modern digital image processing methods, was invented in the 1980s. This is a non-contact, high-precision full-field observation technology. The technology can be used to obtain accurate displacement based on image sub-region matching algorithm by selecting shape function, which can accurately describe the true deformation inside deformation sub-area. The DIC-related software can calculate other deformation parameters based on displacement data. The DIC technology is not only widely used in static rock experiments, but also successfully tested in dynamic rock experiments, such as Split Hopkinson Pressure Bar and blasting tests (Chi et al. 2019; Mansour and Luming 2020; Sharafisafa and Shen 2020).

To obtain the surface displacement of a specimen, it is necessary to obtain a series of speckle images before and after the deformation in the specimen by high-speed camera. After the experiment is completed, the displacement of any deformed stage is calculated by using DIC software by comparing with an undeformed speckle image. The undeformed speckle image is generally referred to as Reference Image, and the deformed speckle image is referred to as Target Image. Assuming that the position coordinates of a pixel is (x, y) in the Reference Image, and the position of the point after the deformation is moved to

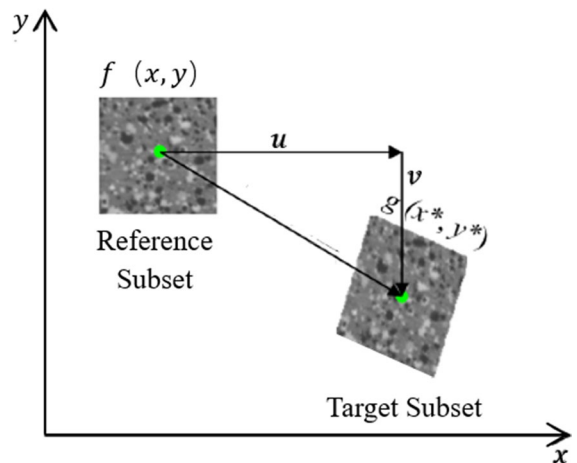


Fig. 1 The calculation process by DIC

(x^*, y^*) , as shown in Fig. 1, the relative displacement of the two points can be expressed by the horizontal displacement component $u(x, y)$ and the vertical displacement component $v(x, y)$, as in Eq. 1. A square area around (x, y) is selected as the reference subset, while the area of the same size around (x^*, y^*) is selected as the target subset in the deformed speckle image. The shape function of the image before and after the deformation is divided into $f(x, y)$ and $g(x^*, y^*)$, since the target subset and the reference subset have certain correlation that can be expressed by the correlation coefficient S in Eq. 2.

$$\begin{aligned} x^* &= x + u(x, y) \\ y^* &= y + v(x, y) \end{aligned} \tag{1}$$

$$S = 1 - \frac{\sum f(x, y) \cdot \sum g(x^*, y^*)}{\sqrt{\sum f^2(x, y) \cdot \sum g^2(x^*, y^*)}} \tag{2}$$

As shown in Fig. 1, the image subset matching algorithm is used to find a target subset centered at (x^*, y^*) , and S is given the minimum value. Then it is considered that the point (x, y) moves to (x^*, y^*) after deformation occurs, and the coordinate difference between the two points is the displacement of the point (x, y) . The strain data on the surface of the test piece can be calculated on the basis of the displacement.

Table 1 Physical–mechanical parameter of the tested sandstone

Physical–mechanical parameter	Value
Uniaxial compressive strength	58.53 MPa
Tensile strength	3.53 MPa
Young's modulus	8.45 GPa
Poisson's ratio	0.245
Density	2200 kg/m ³

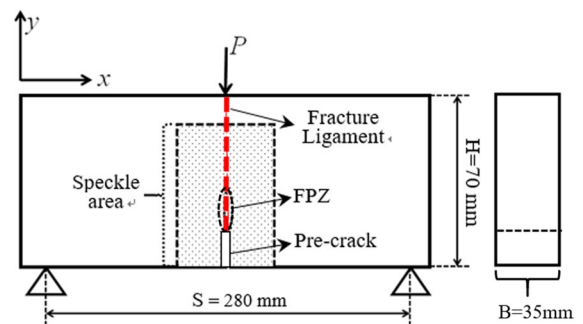
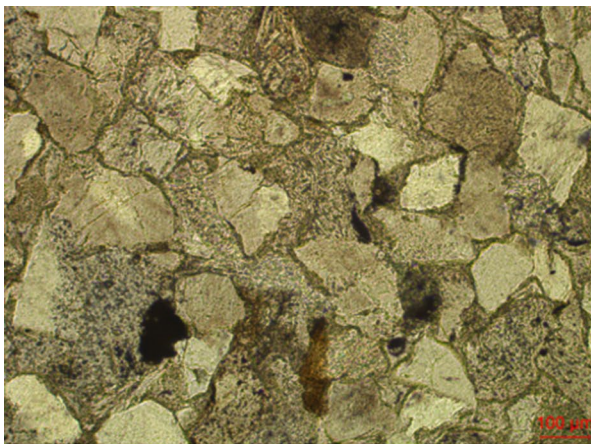
2.2 Three-point Bending Beam Experiment

Three-point bending beams were manufactured from the sandstone in a quarry in Sichuan, China. Physical–mechanical parameters of the tested sandstone are shown in Table 1. Based on the polarizing and transmission micrographs in Fig. 2, the grain size range of the sandstone is shown in Table 2. The sandstone specimens mainly contain quartz, feldspar and calcite. Further analysis by XRD indicates that the proportion of each mineral is 75.34% for SiO₂, 13.84% for Al₂O₃, 3.54% for Fe₂O₃, 2.54% for Na₂O, 2.08% for K₂O, and 0.99% for MgO.

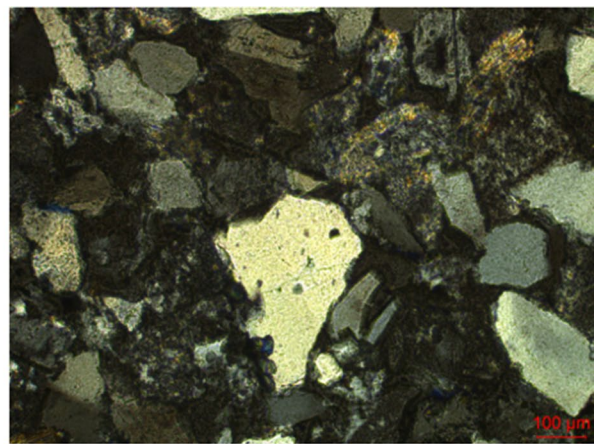
The specimens had a rectangular cross section and a prefabricated central crack, as shown in Fig. 3. The fracture ligament through which the macroscopic crack propagates refers to a specific region between the pre-crack tip and the loading point. The sizes of the specimens are given in Table 3. The load span of

Table 2 Grain size range of the tested sandstone

Grain size (μm)	Quantity	Proportion (%)
100–150	23	9.2
150–200	65	26
200–250	67	26.8
250–300	53	21.2
300–350	27	10.8
350–400	9	3.6
400–450	2	0.8
450–500	1	0.4
500–550	3	1.2
Total	250	100

**Fig. 3** Loading geometry and three-point bending specimen

(a)



(b)

Fig. 2 aTransmission micrograph and b polarizing micrograph

Table 3 Dimensions of specimens

	CNB-1	CNB-2	CNB-3	CNB-4	CNB-5
Length L (mm)	300	299	300	300	299
Height H (mm)	70	70	69	70	69
Thickness B (mm)	35	35	35	35	30
Pre-crack length α (mm)	22	21	22	23	26

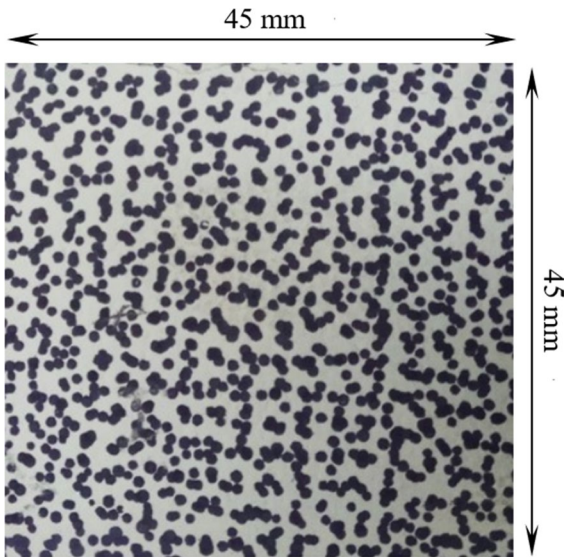


Fig. 4 Speckle pattern

each specimen was $S=280$ mm. The pre-crack was cut by a diamond wire with a diameter of 0.2 mm, resulting in around 0.3 mm crack width.

When speckles were made, watercolor powder was used to make white base film on the specimen surface that was observed during the experiment. Compared with the white paint, the watercolor is non-adhesive and weakly reflective, which improves the quality of images. After the base film was dried, the ink-coated printing plate was pressed to the white base film, and pressed in different directions until the scattered spot area occupied about 50% of the entire base film area. Each of the pure black area and the pure white area should account for 50% of the made speckle pattern. The speckle pattern should have high contrast, non-repetition, and anisotropy, and the gray area should be minimized. The speckle pattern produced in this experiment is shown in Fig. 4.

A high-speed camera named Zeiss was used to acquire the images with 2048×2048 pixels. The

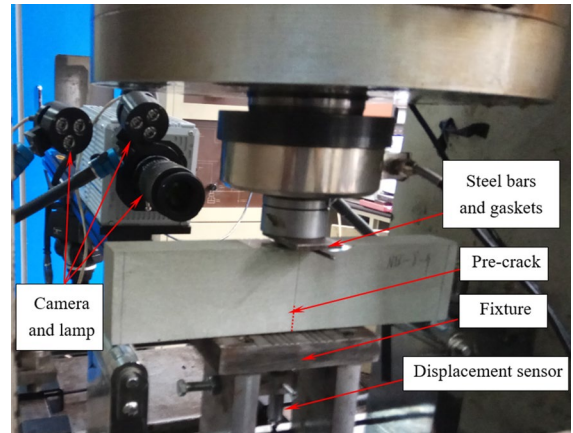


Fig. 5 Loading system for the rock specimen

camera had a 100 mm fixed-focus lens. A image was taken for each 0.001 mm variation in the center deflection of the specimen. Four LED lights were placed on two sides of the camera. The experimental loading system was RMT-150B. To control the whole loading process, the intermediate deflection of the beam was used as a servo feedback signal, and the loading rate was 0.0002 mm/s. The sensor passed through the fixture and directly contacted the specimen. The loading system is shown in Fig. 5.

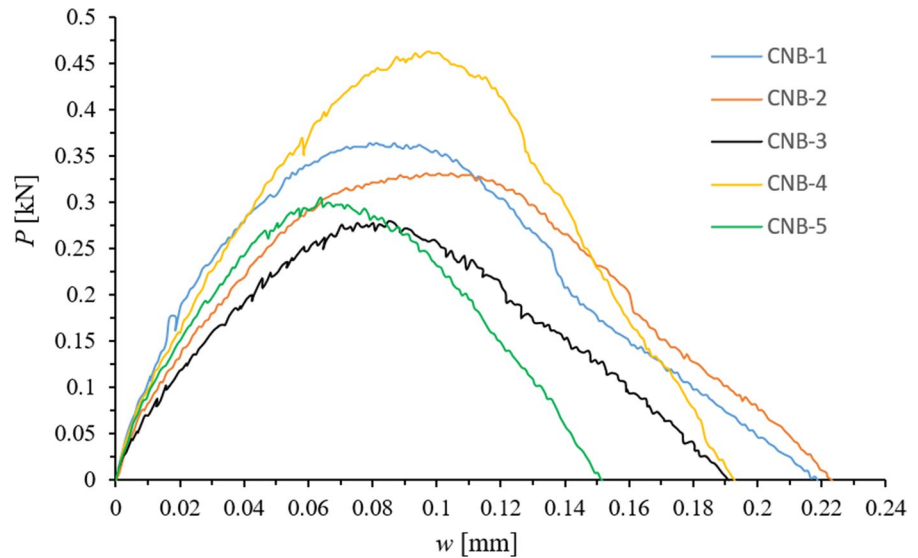
3 Results and Analysis

3.1 Experimental Results

3.1.1 Load-Central Displacement Curve of Specimens

The load–deflection ($P-w$) curves for the specimens are presented in Fig. 6. Notice that in this study the loading process was controlled by the deflection w , i.e. each w value corresponded to one loading stage. As shown in Fig. 6, the load in each specimen increases with an

Fig. 6 Load-deflection in the central of specimen



increasing displacement until the peak load is reached, then it gradually decreases with an increasing displacement, meaning that the fracture ligament of each specimen might be damaged and the elastic modulus weakened. When the load reaches the peak, there is a rough plateau, i.e. the load remains basically unchanged but the displacement continues to increase, and non-linear behavior appears. Although the damage in the ligament may destroy the integrity of the pre-crack's tip, no macro cracks can be seen at the crack tip, because the displacement direction on both sides of the pre-crack does not suddenly change (Fig. 7). Meanwhile, the rock grains still contact and interlock one another which proves the existence of FPZ.

3.1.2 Horizontal Displacement and Strain Contours of the Crack Tip

The collected images from all specimens were processed by software (VIC-2D) to obtain the horizontal displacements and the horizontal strains on the specimens. The software can automatically establish coordinates for the observation area (45 mm × 45 mm). When the software processes the speckle images, the subset and the step are set after considering the image's quality and the data's precision. The subset size is closely related to the accuracy of the data. As the displacement of a pixel is calculated as a data point, the software matches the unloaded subset with the subset after loading to obtain the relevant

point. The more the relevant points are, the better the matching and the displacement accuracy. Therefore, the subset size should be set as large as possible so that more relevant points can be matched to improve the displacement accuracy. In our case, the subset was set to 27 pixels. The step is closely related to the data density and is the number of pixels between two data points. In this study, the step was 4 pixels. The average accuracy allowed was set to 0.05 pixels.

Figure 7 shows the horizontal displacement contours, horizontal strain contours, and horizontal displacements (u) of the ligament at different loading stages. The displacement in the test are reliable, since the error of the displacement in the crack tip region is 0.003–0.008, and crack tip displacement distribution has good repeatability in specimens, as shown in Fig. 7. Each set of tests has five specimens. The results for all specimens are not shown in the manuscript, however, conclusions are drawn based on the results of all specimens. The horizontal direction is the x-axis, the displacement to the right is positive and vice versa. The vertical direction is the y-axis. On the same contour line, the horizontal displacement or strain values is in the same level, and difference between two adjacent contour lines is equal. Therefore, the density of contours reflects the gradient of horizontal displacement and strain. The horizontal displacement contours near the crack tip are dense and diverge around the crack tip. The displacement difference on both sides of crack tip is 28 μm

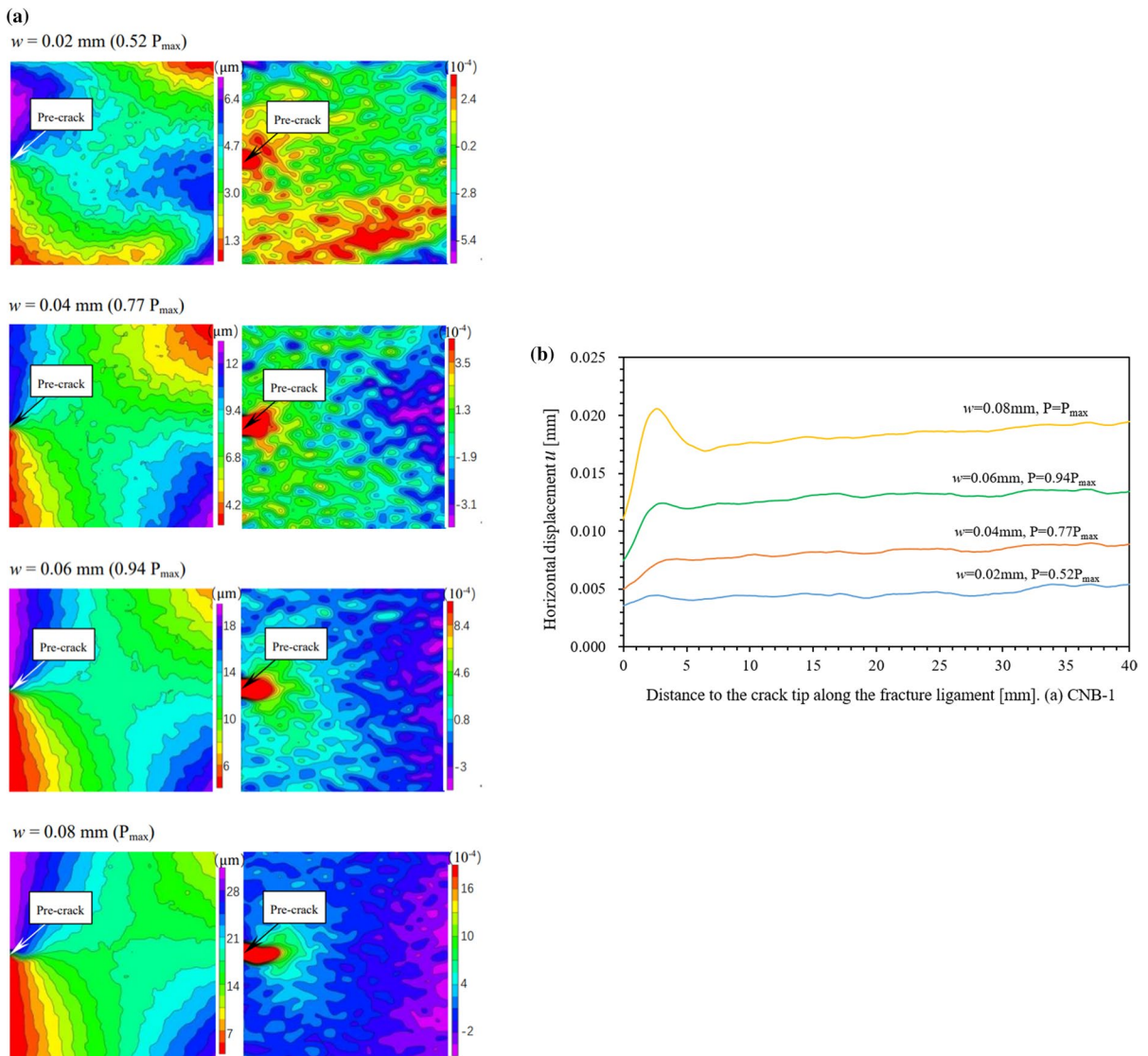


Fig. 7 Horizontal displacement and strain contours, and horizontal displacements of the ligament at different loading stages

for CNB-1, 44 μm for CNB-2, and 32 μm for CNB-4 at the peak. The strain variation within 7 mm in the y-axis direction close to crack tip is 6×10^{-4} for CNB-1, 5×10^{-3} for CNB-2, and 7.6×10^{-4} for CNB-4. The strain of crack tip is 25% of the total deformation of the entire ligament, but the length of the crack tip is only 12.5% of the entire ligament length. Through the horizontal strain contours, the deformation of the

specimen can be intuitively observed. In brief, the crack tip has relatively serious deformation.

3.2 Initiation and Development of FPZ

According to the characteristics of displacement jump in CZM (Yang and Cox 2005; Sarris and Papanastasiou 2011), a fluctuation coefficient is proposed to determine the boundary of the FPZ. The fluctuation

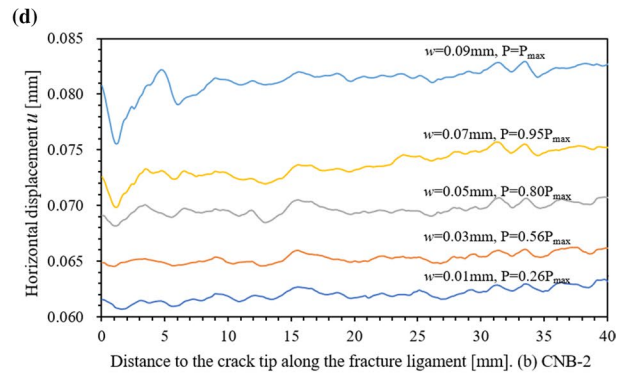
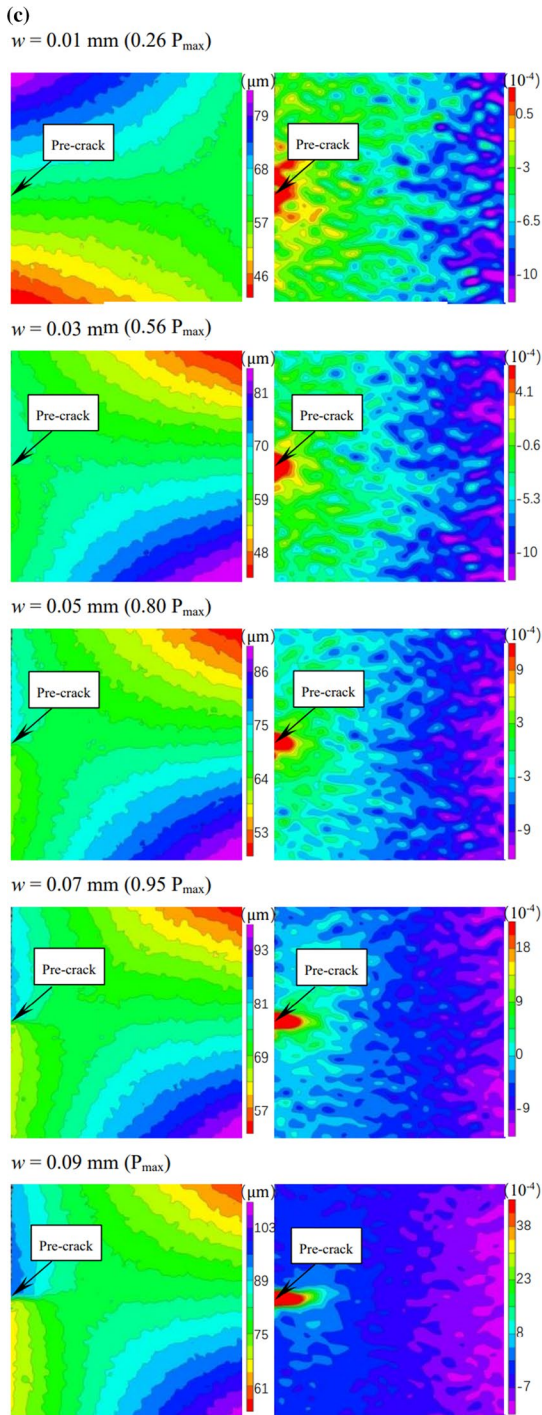


Fig. 7 (continued)

coefficient is defined as a function of the horizontal displacement of five adjacent data points, as shown in

Eq. 3. This is the first step to identify the threshold value.

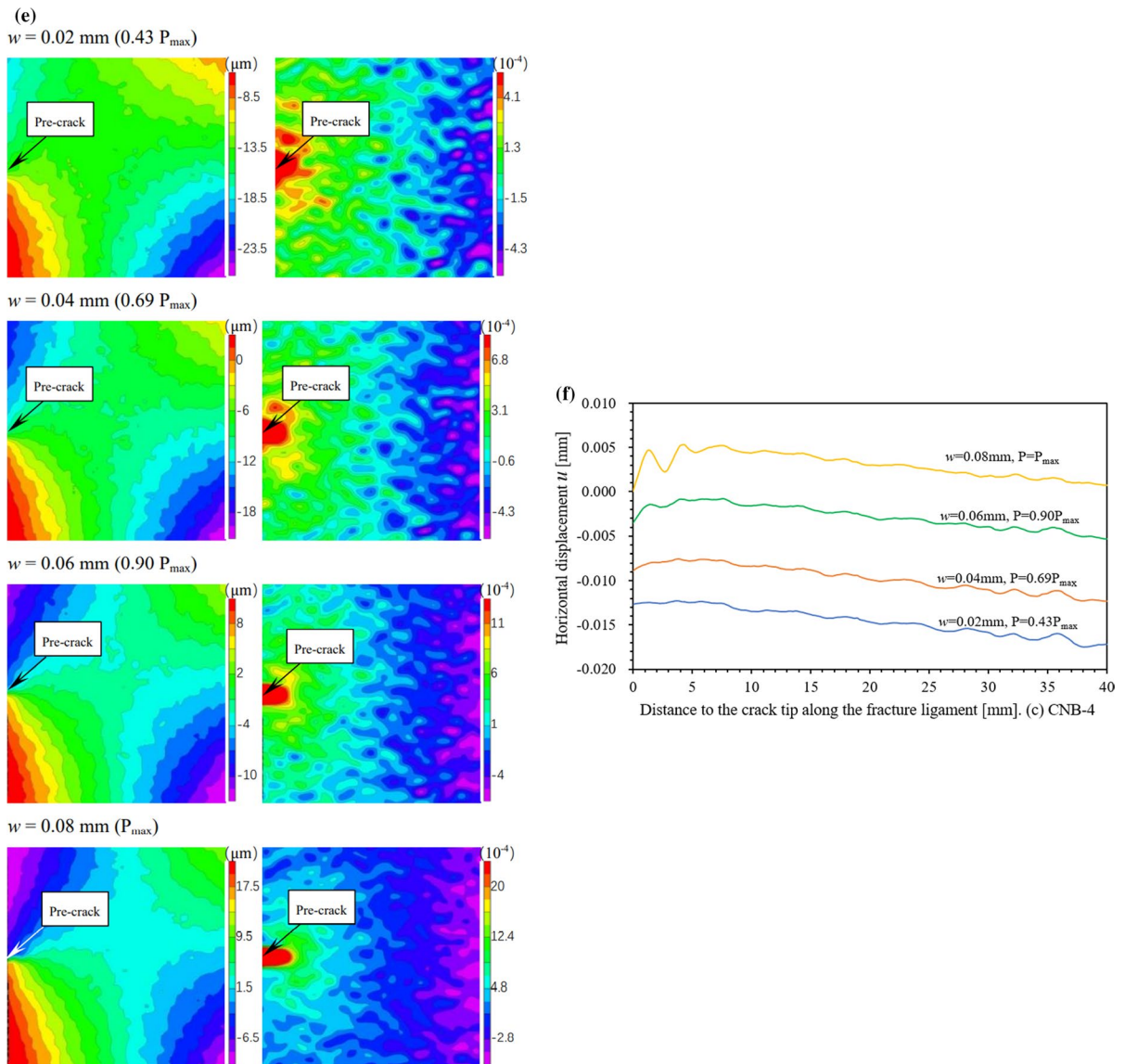


Fig. 7 (continued)

$$\lambda_i = \sqrt{\sum_{n=i-2}^{i+2} (u_n - u)^2} \tag{3}$$

where λ_i is the fluctuation coefficient of the data point i , u_n is the horizontal displacement value of the n -th data point, u is the average of five consecutive horizontal displacement values, and n is the horizontal displacement sequence number of the data point.

Second step: suitable loading moments are selected (in this paper, five loading moments are chosen) and the distribution curve of the fluctuation coefficient is plotted along the fracture ligament from the crack tip. One may observe a sharp increase of the fluctuation coefficient near the tip at a moment, and the fluctuation coefficient in the crack tip region is larger than that in other regions

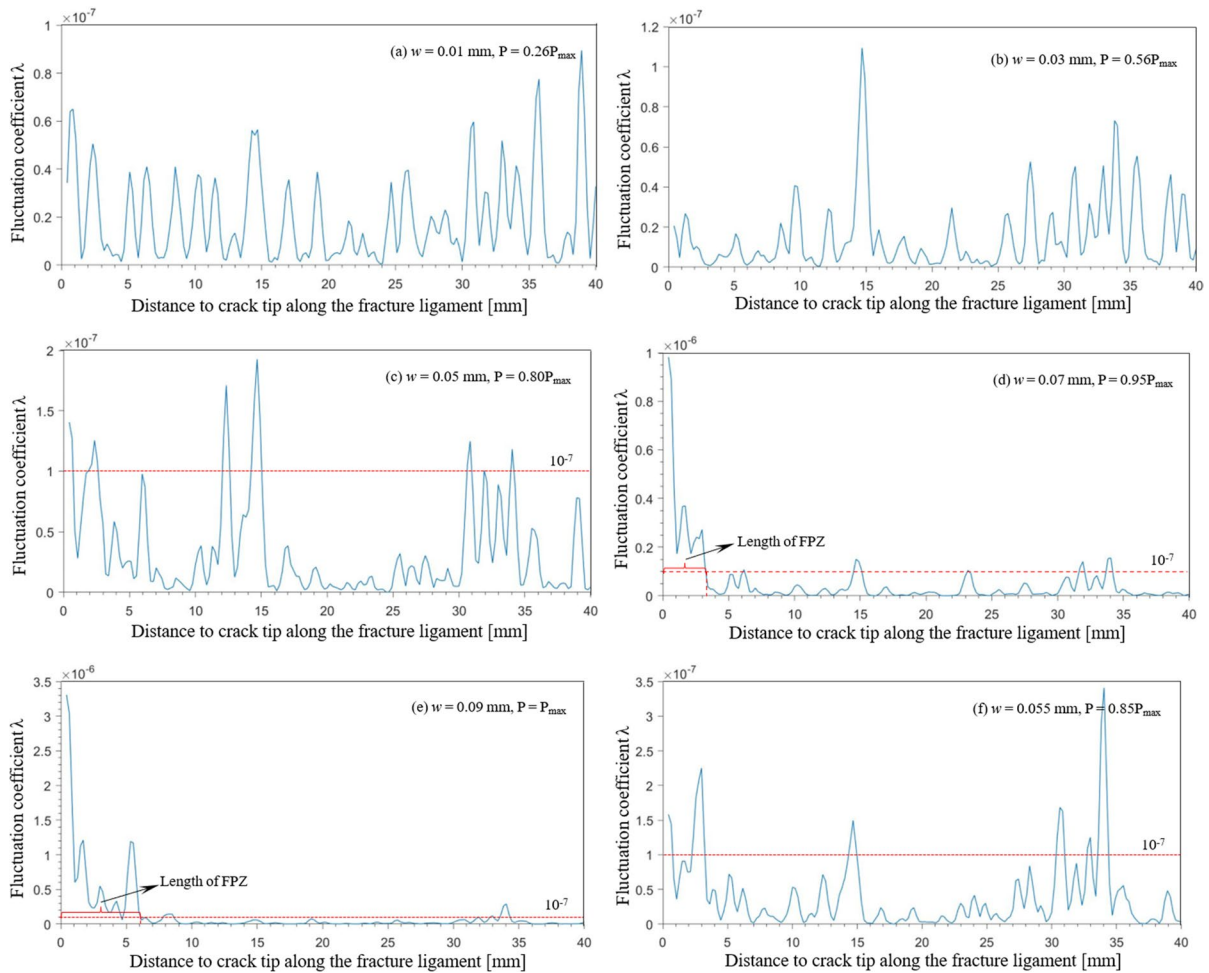


Fig. 8 Fluctuation coefficient distribution along fracture ligament at different loading stages

of the fracture ligament. Then one can choose the least fluctuation coefficient as the threshold value.

Last step: According to the actual situation, the threshold value can be fine-tuned. The principle of fine-tuning is to ensure that the threshold value is greater than the fluctuation coefficients of most regions away from the crack tip.

In this study, a coordinate is established taking the crack tip as the origin, and the distance to the crack tip along the fracture ligament is consistent with the corresponding coordinate values. Figure 8a–c indicates that the fluctuation coefficient of the fracture ligament is below the order of 10^{-7} before $0.8 P_{\max}$ ($w=0.05$ mm). When the load is up to $0.95 P_{\max}$ (Fig. 8d), the fluctuation coefficient near the crack tip suddenly exceeds 10^{-7} and even reaches 10^{-6} .

However, the fluctuation coefficient in the other regions of the fracture ligament is still below the order of 10^{-7} . Thus, 10^{-7} was taken as the critical value to determine FPZ initiation. The FPZ was initiated in the $0.80\text{--}0.95 P_{\max}$ for CNB-2.

The advantage of the fluctuation coefficient method is that it clearly shows the length boundary of FPZ, as shown in Fig. 8d. In addition, the displacement fluctuation coefficient method can amplify the variation of displacement, as shown in the comparison of the original displacement (Fig. 7d) with the fluctuation coefficients (Fig. 8d).

The above description indicates that the FPZ was initiated at $P=0.80\text{--}0.95 P_{\max}$. In order to determine the initiation stage of FPZ more accurately, the fluctuation coefficient along the fracture ligament for

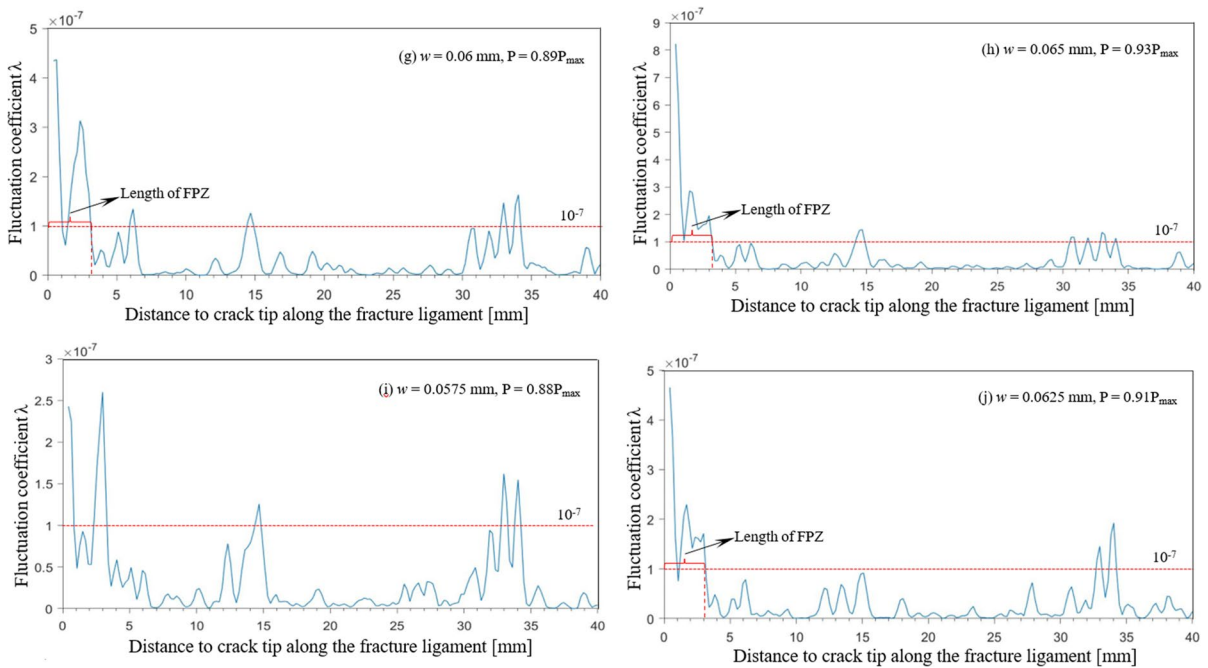


Fig. 8 (continued)

CBN-2 is calculated at $w=0.0550$ mm ($0.85 P_{max}$), $w=0.0600$ mm ($0.89 P_{max}$), and $w=0.0650$ mm ($0.93 P_{max}$), as shown in Fig. 8f–h.

Although Fig. 8f indicates that the fluctuation coefficient at 0–0.7 mm and 2.2–3.1 mm reaches the order of 10^{-7} at $w=0.0550$ mm ($0.85 P_{max}$), the two regions are separate and their total length is 1.6 mm which is almost equal to the length of the region (0.7–2.2 mm) between the two separated regions. The fluctuation coefficient at 0.7–2.2 mm is below the order of 10^{-7} . Therefore, the FPZ does not initiate at $w=0.055$ mm ($0.85 P_{max}$). When the load reaches $0.89 P_{max}$ (Fig. 8g), the region where the fluctuation coefficient is above the order 10^{-7} is around 3 mm in the ligament. Although 0.5 mm ligament does not reach the order 10^{-7} in the region, considering that the average fluctuation coefficient of this 0.5 mm ligament is 0.9×10^{-7} , it can be determined that the FPZ was initiated at $w=0.060$ mm ($0.89 P_{max}$) for CNB-2. Similarly, the FPZ was initiated at $P=0.77–0.94 P_{max}$ for CNB-1 and at $P=0.69–0.90 P_{max}$ for CBN-4.

To confirm the determined initiation stage of FPZ, the fluctuation coefficient close to this initiation stage ($0.89 P_{max}$, $w=0.060$ mm) is calculated at $w=0.0575$ mm ($0.88 P_{max}$), $w=0.0625$ mm (0.91

P_{max}), as shown in Fig. 8i, j. The distribution of fluctuation coefficient along the ligament at $0.88 P_{max}$ (Fig. 8i) is similar to that at $0.85 P_{max}$ (Fig. 8f). The regions where the coefficient reaches the order of 10^{-7} are discontinuous. The distribution of fluctuation coefficient along the ligament at $0.91 P_{max}$ (Fig. 8j) is almost the same as that at $0.89 P_{max}$ (Fig. 8g). The region where the fluctuation coefficient was above the order 10^{-7} is also around 3 mm. Compared with $0.88 P_{max}$, the region below the order of 10^{-7} decreased. Therefore, it can be concluded that the FPZ was initiated at $0.89 P_{max}$ ($w=0.060$ mm) for CNB-2.

In brief, as an FPZ is initiated, the fluctuation of the horizontal displacement near the crack tip is significantly greater than that in other regions of the fractured ligament. When the fluctuation coefficient reaches the order of 10^{-7} near the crack tip, the FPZ is initiated. The initiation stage of FPZ is between $w=0.0575$ mm ($0.88 P_{max}$) and $w=0.060$ mm ($0.89 P_{max}$) for CNB-2, between $w=0.040$ mm ($0.77 P_{max}$) and $w=0.045$ mm ($0.83 P_{max}$) for CNB-1, and between $w=0.050$ mm ($0.81 P_{max}$) and $w=0.055$ mm ($0.86 P_{max}$) for CNB-4, respectively.

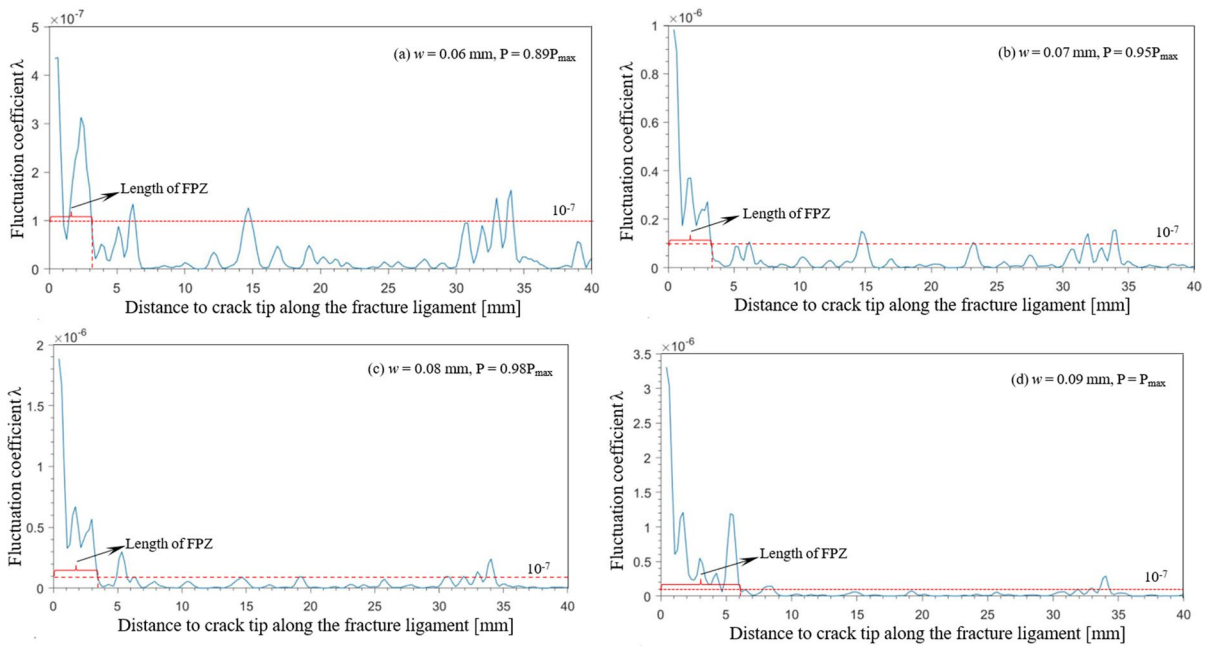


Fig. 9 Fluctuation coefficient distribution along fracture ligament at different loading stages

3.3 Size Development of FPZ and Deformation Analysis of Fracture Ligament

The sizes of FPZ include two parameters, length and width in 2D condition. The length variation of FPZ is of great significance for evaluating the damage near the crack tip. Four-loading stages are selected to study the FPZ development: $w = 0.06$ mm ($0.89 P_{max}$), $w = 0.07$ mm ($0.95 P_{max}$), $w = 0.08$ mm ($0.98 P_{max}$) and $w = 0.09$ mm (P_{max}). The calculated fluctuation coefficient along the fracture ligament is shown in Fig. 9a–d for CNB-2.

Figure 9a–c shows the length of FPZ is maintained at about 3.2 mm before $w = 0.08$ mm ($0.98 P_{max}$) for CNB-2. The fluctuation coefficient in the FPZ increases from 4.4×10^{-7} at $0.89 P_{max}$ to 1.8×10^{-6} at $0.98 P_{max}$ for CNB-2. However, the fluctuation coefficient varies in a small range outside the FPZ along the fracture ligament (Fig. 9a–c). When the load reaches the peak value (Fig. 9d), the fluctuation coefficient increases to 1.2×10^{-6} , 4 times greater than the fluctuation coefficient 3×10^{-7} at $0.98 P_{max}$ (Fig. 9c) at a distance of 5.5 mm from the crack tip, making the FPZ length rapidly increase from 3.4 to 6.1 mm. Figure 10

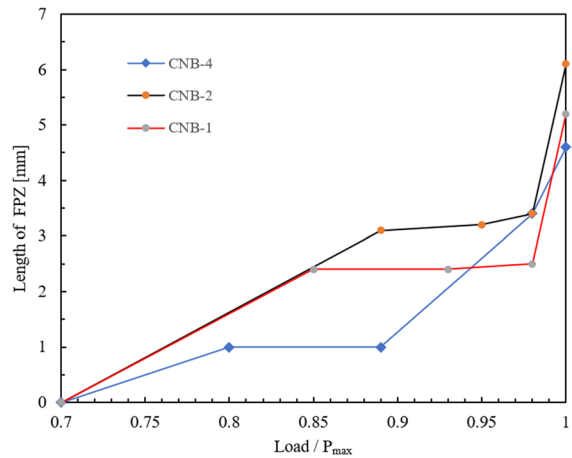


Fig. 10 Development trend of FPZ’s length with increasing load

shows that the development of FPZ have similar trends in other specimens.

To present the deformation along the fracture ligament quantitatively during FPZ development, the horizontal strain values along the fracture ligament are shown in Fig. 11 at different loading stages. Figure 11 indicates that the horizontal strain values increase

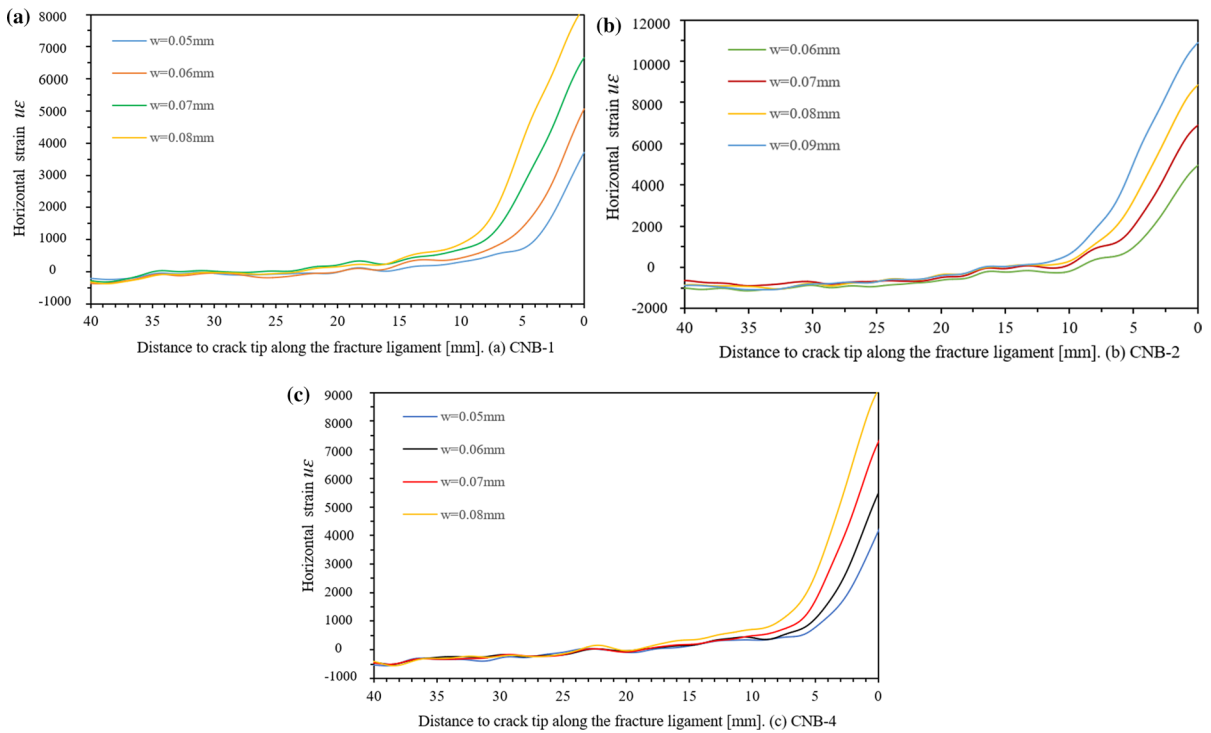


Fig. 11 Horizontal strain distribution along fracture ligament

rapidly with a decreasing distance (from 10 to 0 mm) to the crack tip.

Figure 11 shows that the strains along the ligament increase rapidly as the distance to the crack tip decreases. The main reason is that more microcracks might be induced near the crack tip with the increasing load, and the microcrack-caused damage is accumulated. In Fig. 11, it can be found that the strain at the front end of FPZ is about 3000–4000 $\mu\epsilon$, and the strain at the rear end of FPZ is about 8000–11000 $\mu\epsilon$.

The strain variation $\Delta\epsilon$ per unit length of fracture ligament ΔL , $\frac{\Delta\epsilon}{\Delta L}$, is used to show the changes of strain in the fracture ligament at different loading stages for specimen CNB-2, as shown in Fig. 12.

Figure 12 shows that the horizontal-strain variation per unit length of fracture ligament is close to zero in the ligament 40–13 mm away from the crack tip. This region is defined as low-stress elastic zone. The stress state of the fractured ligament gradually changes from compressive stress to tensile stress in low-stress elastic zone (Fig. 12). The horizontal-strain variation curve starts to rise sharply at one point which is

defined as the rising point of the curve, but when the curve enters the FPZ, it goes downward, i.e. the horizontal-strain gradient value decreased (Fig. 12). The region from the rising point to the FPZ can be defined as stress concentration zone where most of the elastic energy is stored. In summary, the entire fracture ligament can be divided into low-stress elastic zone, stress concentration zone and FPZ.

4 Discussion

4.1 On FPZ

In this study, the initiation of FPZ was directly determined by the displacement values, and the initiation of FPZ occurred at 77–89% peak load, which is within the range of 70–90% peak load obtained by Dutler et al. (2018) and Nathan et al. (2018). The length of FPZ is 4.6–6.1 mm at the peak load in the study. This result is consistent with the previous experiment results by Lin and Labuz (2013),

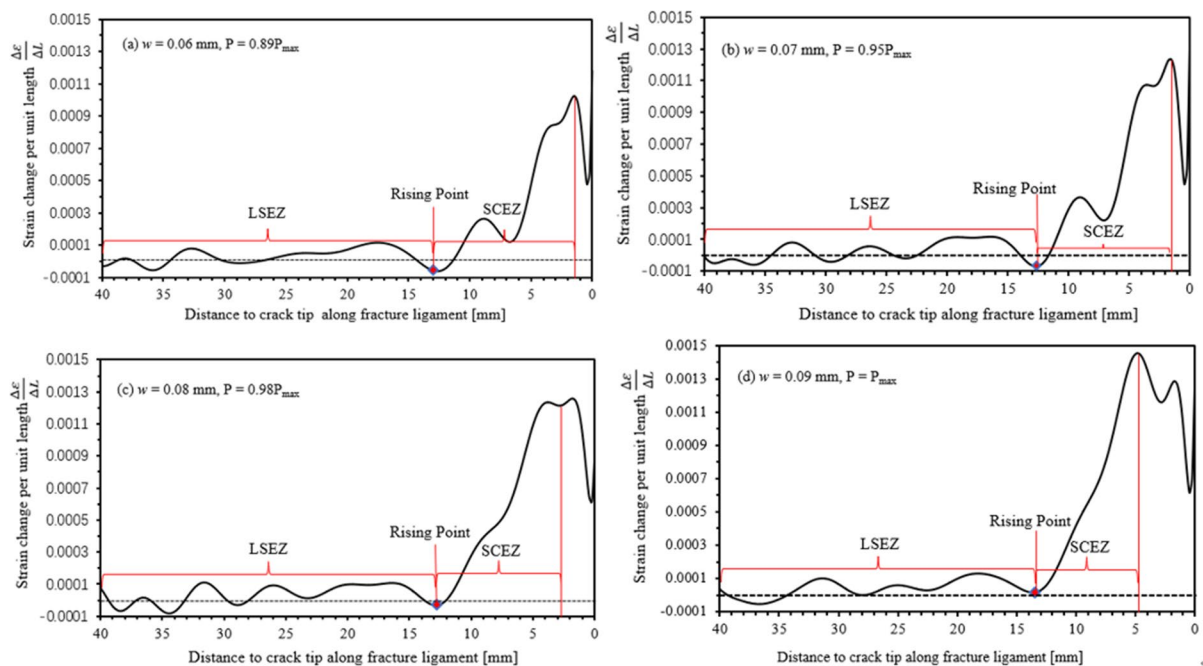


Fig. 12 Horizontal strain variation per unit length along the fracture ligament of CNB-2

Lin et al. (2014) who found that the length of FPZ was 5–7 mm for sandstone. Zhang et al. (2021a, b) used SCB specimens with diameters of 50 100 150 200 mm to measure the corresponding FPZ lengths with mean values of 4.05, 7.59, 10.62 and 12.87 mm. They also found that the range of the FPZ reaches the maximum at the peak. The closer to the peak, the faster the development of the FPZ, and the length of the FPZ that increases from 90% pre-peak to peak accounts for 50% of the total FPZ length. The FPZ length of specimens of different sizes at the peak is about 2–2.5 times the width (Zhang et al. 2021a, b). In order to validate the experimental results for the sizes of FPZ, the horizontal displacement from the numerical simulations is compared with the experimental results (Fig. 13). The distribution trend and magnitude of displacement in this experiment is consistent with in the PFC.

This study on FPZ is limited to quasi-static loading conditions. It is necessary to investigate FPZ under dynamic loading conditions in which crack branching and layer cracks are found (Zhang et al. 2000, 2001). Such crack branching or layer cracks might be one of the sources of the fine materials or particles from rock blasting (Zhang et al. 2020a,b; Fournay 2015;

Ouchterlony and Moser 2012). Therefore, it is interesting to investigate the FPZ under dynamic loading conditions in the future.

4.2 Applications

(1) Study on mechanism of rock bursts.

Experiments in this study showed that the FPZ rapidly grew as the load approached the peak load, as shown in Fig. 10, and then one macrocrack was generated (based on the DIC result) and the load decreased. Since the strains in the FPZ of a rock specimen are extremely higher than other areas in the specimen, see Figs. 7 and 11, the FPZ must store much energy. When a rock burst occurs, part or most of the stored energy might be released as kinetic energy to eject fractured rock. Such a process may be studied by more laboratory tests with more rock types using a similar experiment method as in this study.

(2) Fines in rock blasting.

Since ultra-fine mineral particles are usually difficult to recovered by most mineral processing techniques (Wills and Finch 2015 and Schimek et al. 2012), a vast amount of minerals resources, including

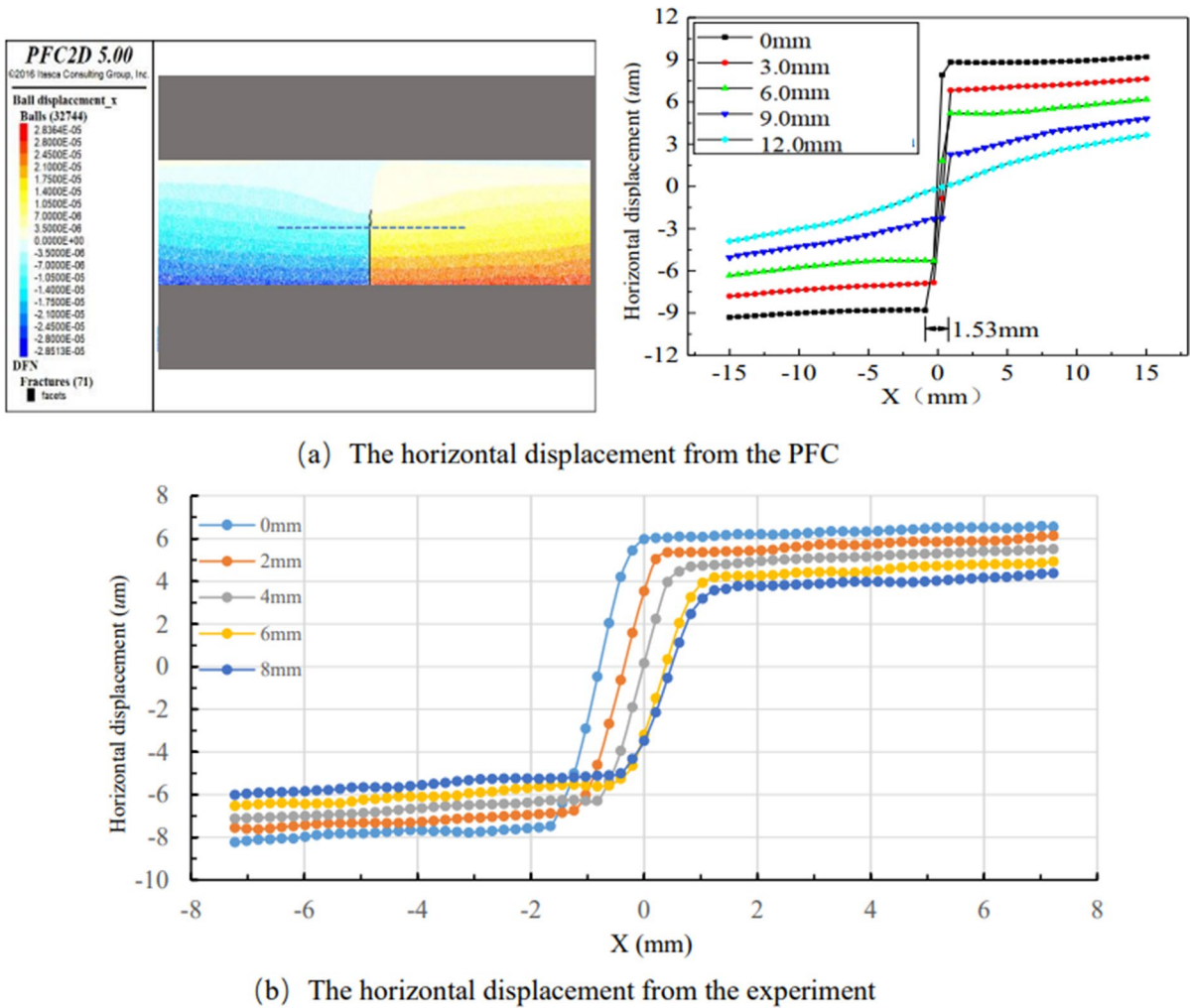


Fig. 13 The displacement comparison between the PFC and experiment

such fines, are lost every year (Zhang et al. 2021a, b). At the same time, the worldwide production of fines wastes a vast amount of energy (Zhang and Ouchterlony 2022). Fines come from not only the crushed zone but also crack branching during rock fracture by blasting or stress wave loading (Reichholf 2003; Zhang et al. 2021a, b; Fourney 2015; Schimek et al. 2012). The measurement by Reichholf (2003) showed that around 50% weight of the material smaller 1 mm was generated within the crushed zone of blasthole, meaning that other 50% fine particles were not from the crushed zone. A possible source of the fine particles is the FPZs at the tips of the cracks produced by blasting. Thus, it will be useful to investigate the

relationship between the FPZ and the fine particle production in rock fracture in the future.

5 Conclusions

The loading stage when an FPZ is initiated is between 77 and 89% peak load. As the FPZ is initiated, the fluctuation coefficient of horizontal displacement reaches the order of 10^{-7} around the crack tip.

The initial length of the FPZ is about 1.0–3.1 mm, and the length of the FPZ is 4.6–6.1 mm at the peak load. The FPZ does not gradually increase from zero, and its initial length is about 21.7–51.7% of the length at the peak load. The fluctuation coefficient increases

gradually in the FPZ, but it remains nearly a constant in the region far from the FPZ. As the peak load is approached, the length of FPZ suddenly increases.

The entire fracture ligament can be divided into low-stress elastic zone, stress concentration elastic zone and FPZ. The strain value is maintained between -1000 and $-500 \mu\epsilon$ in the low-stress elastic zone and between 500 and $3000 \mu\epsilon$ in the stress concentration elastic zone. The strain at the front end of the FPZ is maintained at about 3000 – $4000 \mu\epsilon$ during the FPZ development, but the strain at the rear end of the FPZ increases with increasing load and reaches 8000 – $11000 \mu\epsilon$ at the peak load.

Author Contributions Material preparation, data collection and analysis were performed by Yang Qiao. The first draft of the manuscript was written by Yang Qiao and all authors commented on previous versions of the manuscript. All authors read and approved the final manuscript.

Funding Open Access funding provided by University of Oulu. This study was supported by K. H. Renlund Foundation in Finland. The first author is grateful to the CSC (China Scholarship Council) for the financial support.

Data Availability The datasets generated during the current study are not publicly available, but are available from the corresponding author on reasonable request.

Conflict of Interest The authors have no relevant financial or non-financial interests to disclose.

Open Access This article is licensed under a Creative Commons Attribution 4.0 International License, which permits use, sharing, adaptation, distribution and reproduction in any medium or format, as long as you give appropriate credit to the original author(s) and the source, provide a link to the Creative Commons licence, and indicate if changes were made. The images or other third party material in this article are included in the article's Creative Commons licence, unless indicated otherwise in a credit line to the material. If material is not included in the article's Creative Commons licence and your intended use is not permitted by statutory regulation or exceeds the permitted use, you will need to obtain permission directly from the copyright holder. To view a copy of this licence, visit <http://creativecommons.org/licenses/by/4.0/>.

References

- Barenblatt GI (1962) The mathematical theory of equilibrium cracks in brittle fracture. *Adv Appl Mech* 7(2):55–129. [https://doi.org/10.1016/S0065-2156\(08\)70121-2](https://doi.org/10.1016/S0065-2156(08)70121-2)
- Bazant ZP (1976) Instability, ductility, and size effect in strain-softening concrete. *ASCE J Eng Mech Div* 102:331–344
- Bieniawski ZT (1968) Fracture dynamics of rock. *Int J Fract Mech* 4:415–430
- Brooks Z, Ulm FJ, Einstein HH (2013) Environmental scanning electron microscopy (ESEM) and nanoindentation investigation of the crack tip process zone in marble. *Acta Geotech* 8:223–245. <https://doi.org/10.1007/s11440-013-0213-z>
- Chi LY, Zhang ZX, Aalberg A et al (2019) Fracture processes in granite blocks under blast loading. *Rock Mech Rock Eng* 52:853–868. <https://doi.org/10.1007/s00603-018-1620-0>
- Dong J, Chen M, Jin Y et al (2019) Study on micro-scale properties of cohesive zone in shale. *Int J Solids Struct* 163:178–193. <https://doi.org/10.1016/j.ijsolstr.2019.01.004>
- Dugdale DS (1960) Yielding of steel sheets containing slits. *J Mech Phys Solids* 8(2):100–104. [https://doi.org/10.1016/0022-5096\(60\)90013-2](https://doi.org/10.1016/0022-5096(60)90013-2)
- Dutler N, Nejati M, Valley B et al (2018) On the link between fracture toughness, tensile strength, and fracture process zone in anisotropic rocks. *Eng Fract Mech* 201:8–24. <https://doi.org/10.1016/j.engfracmech.2018.08.017>
- Evans AG, Fuller ER (1974) Crack propagation in ceramic materials under cyclic loading conditions. *Metall Trans* 5:27–33. <https://doi.org/10.1007/BF02642921>
- Fakhimi A, Tarokh A (2013) Process zone and size effect in fracture testing of rock. *Int J Rock Mech Min Sci* 60:59–80. <https://doi.org/10.1016/j.ijrmms.2012.12.044>
- Fakhimi A, Tarokh A, Labuz JF (2017) Cohesionless crack at peak load in a quasi-brittle material. *Eng Fract Mech* 179:272–277. <https://doi.org/10.1016/j.engfracmech.2017.05.012>
- Fourney WL (2015) The Role of stress waves and fracture mechanics in fragmentation. *Blast Fragm* 9(2):83–106
- Friedman M, Handin J, Alani G (1972) Fracture-surface energy of rocks. *Int J Rock Mech Min Sci* 9:757–764
- Garg P, Pandit B, Hedayat A et al (2021) An integrated approach for evaluation of linear cohesive zone model's performance in fracturing of rocks. *Rock Mech Rock Eng* 55:2917–2936. <https://doi.org/10.1007/s00603-021-02561-5>
- Ghamgosar M, Erarslan N (2016) Experimental and numerical studies on development of fracture process zone (FPZ) in rocks under cyclic and static loadings. *Rock Mech Rock Eng* 49:893–908. <https://doi.org/10.1007/s00603-015-0793-z>
- Hillerborg A, Modéer M, Petersson P-E (1976) Analysis of crack formation and crack growth in concrete by means of fracture mechanics and finite elements. *Cem Concr Res* 6:773–781. [https://doi.org/10.1016/0008-8846\(76\)90007-7](https://doi.org/10.1016/0008-8846(76)90007-7)
- Hu X, Duan K (2008) Size effect and quasi-brittle fracture: the role of FPZ. *Int J Fract* 154:3–14. <https://doi.org/10.1007/s10704-008-9290-7>
- Justo J, Castro J, Cicero S et al (2017) Notch effect on the fracture of several rocks: application of the theory of critical distances. *Theor Appl Fract Mech* 90:251–258. <https://doi.org/10.1016/j.tafmec.2017.05.025>
- Kaminsky A, Kipnis L, Dudik M (2004a) Initial development of the prefraction zone near the tip of a crack reaching the interface between dissimilar media. *Int Appl Mech*

- 2:176–182. <https://doi.org/10.1023/b:inam.0000028596.95084.ce>
- Kaminsky A, Kipnis L, Dudik M (2004b) Modeling of the crack tip plastic zone by two slip lines and the order of stress singularity. *Int J Fract* 127(1):105–109. <https://doi.org/10.1023/b:frac.0000035083.26389.db>
- Labuz JF, Shah SP, Dowding CH (1985) Experimental analysis of crack propagation in granite. *Int J Rock Mech Min Sci* 22:85–98
- Labuz JF, Shah SP, Dowding CH (1987) The fracture process zone in granite: evidence and effect. *Int J Rock Mech Min Sci* 24:235–246. [https://doi.org/10.1016/0148-9062\(87\)90178-1](https://doi.org/10.1016/0148-9062(87)90178-1)
- Lin Q, Labuz JF (2013) Fracture of sandstone characterized by digital image correlation. *Int J Rock Mech Min Sci* 60:235–245. <https://doi.org/10.1016/j.ijrmms.2012.12.043>
- Lin Q, Yuan H, Biolzi L, Labuz JF (2014) Opening and mixed mode fracture processes in a quasi-brittle material via digital imaging. *Eng Fract Mech* 131:176–193. <https://doi.org/10.1016/j.engfracmech.2014.07.028>
- Maji AK, Wang JL (1992) Experimental study of fracture processes in rock. *Rock Mech Rock Eng* 25:25–47. <https://doi.org/10.1007/BF01041874>
- Mansour S, Luming S (2020) Experimental investigation of dynamic fracture patterns of 3D printed rock-like material under impact with digital image correlation. *Rock Mech Rock Eng* 53:3589–2607
- Nathan D, Morteza N, Benoît V, Florian A, Giulio M (2018) On the link between fracture toughness, tensile strength, and fracture process zone in anisotropic rocks. *Eng Fract Mech* 201:56–79. <https://doi.org/10.1016/j.engfracmech.2018.08.017>
- Orowan E (1949) Fracture and strength of solids. *Rep Prog Phys* 12:34–157
- Ouchterlony F (1982) Review of fracture toughness testing of rock. *SM Archives* 7:145–159. [https://doi.org/10.1016/0148-9062\(81\)90541-6](https://doi.org/10.1016/0148-9062(81)90541-6)
- Ouchterlony F, Moser P (2012) *Rock fragmentation by blasting*. CRC Press, London
- Qiao Y, Zhang S (2020) Test method of determination of rock fracture process zone. *J Exp Mech* 2:287–299
- Reichholf G (2003) Experimental investigation into the characteristic of particle size distributions of blasted material. In: Doctoral thesis, Montanuniversität Leoben.
- Rice JR (1964) A path independent integral and the approximate analysis of strain concentration by notches and cracks. *J Appl Mech Trans ASME* 35(2):379–386. <https://doi.org/10.1115/1.3601206>
- Sarris E, Papanastasiou P (2011) The influence of the cohesive process zone in hydraulic fracturing modelling. *Int J Fract* 167:33–45. <https://doi.org/10.1007/s10704-010-9515-4>
- Schimek P, Ouchterlony F, Moser P (2012) *Measurement and analysis of blast fragmentation*. CRC Press, London
- Schmidt RA (1980) A microcrack model and its significance to hydraulic fracturing and fracture toughness testing. In Paper presented at the The 21st U.S. Symposium on Rock Mechanics (USRMS), Rolla, Missouri
- Schmidt RA, Lutz TJ (1979) K_{Ic} and J_{Ic} of Westerly granite—effects of thickness and in-plane dimensions. *American Soc Test Mater*
- Sharafisafa M, Shen L (2020) Experimental investigation of dynamic fracture patterns of 3D printed rock-like material under impact with digital image correlation. *Rock Mech Rock Eng* 53:3589–3607. <https://doi.org/10.1007/s00603-020-02115-1>
- Tarokh A, Makhnenko RY, Fakhimi A, Labuz JF (2017) Scaling of the fracture process zone in rock. *Int J Fract*. <https://doi.org/10.1007/s10704-016-0172-0>
- Turon A, Dávila CG, Camanho PP, Costa J (2007) An engineering solution for mesh size effects in the simulation of delamination using cohesive zone models. *Eng Fract Mech* 74(10):1665–1682. <https://doi.org/10.1016/j.engfracmech.2006.08.025>
- Vavro L, Souček K, Kytýř D et al (2017) Visualization of the evolution of the fracture process zone in sandstone by transmission computed radiography. *Proc Eng* 191:689–696. <https://doi.org/10.1016/j.proeng.2017.05.233>
- Veselý V, Frantík P (2014) An application for the fracture characterisation of quasi-brittle materials taking into account fracture process zone influence. *Adv Eng Softw* 72:66–76. <https://doi.org/10.1016/j.advengsoft.2013.06.004>
- Whittaker BN, Singh RN, Sun G (1992) *Rock fracture mechanics. Principles, design and applications*. Elsevier Science Publishers B.V., Amsterdam (Netherlands)
- Willett T, Josey D, Lu RXZ et al (2017) The micro-damage process zone during transverse cortical bone fracture: No ears at crack growth initiation. *J Mech Behav Biomed Mater* 74:371–382. <https://doi.org/10.1016/j.jmbbm.2017.06.029>
- Wills BA, Finch JA (2015) *Wills' mineral processing technology: An introduction to the practical aspects of ore treatment and mineral recovery*. Butterworth-Heinemann, Oxford
- Wu J, Gao J, Feng Z et al (2020) Investigation of fracture process zone properties of mode I fracture in heat-treated granite through digital image correlation. *Eng Fract Mech* 235:71–92. <https://doi.org/10.1016/j.engfracmech.2020.107192>
- Yang Q, Cox B (2005) Cohesive models for damage evolution in laminated composites. *Int J Fract* 133:107–137
- Zhang S, Wang H, Li X et al (2021a) Experimental study on development characteristics and size effect of rock fracture process zone. *Eng Fract Mech* 241:107–116. <https://doi.org/10.1016/j.engfracmech.2020.107377>
- Zhang ZX, Hou DF, Aladejare A et al (2021b) World mineral loss and possibility to increase ore recovery ratio in mining production. *Int J Min Reclam Environ* 35:670–691. <https://doi.org/10.1080/17480930.2021.1949878>
- Zhang ZX, Hou DF, Guo Z et al (2020a) Experimental study of surface constraint effect on rock fragmentation by blasting. *Int J Rock Mech Min Sci* 128:257–278. <https://doi.org/10.1016/j.ijrmms.2020.104278>
- Zhang ZX, Hou DF, Guo Z, He Z (2020b) Laboratory experiment of stemming impact on rock fragmentation by a high explosive. *Tunn Undergr Space Technol* 97:103–104. <https://doi.org/10.1016/j.tust.2019.103257>
- Zhang ZX, Kou SQ, Jiang LG, Lindqvist PA (2000) Effects of loading rate on rock fracture: fracture characteristics and energy partitioning. *Int J Rock Mech Min Sci* 37:745–762. [https://doi.org/10.1016/s1365-1609\(00\)00008-3](https://doi.org/10.1016/s1365-1609(00)00008-3)

- Zhang ZX, Ouchterlony F (2022) Energy requirement for rock breakage in laboratory experiments and engineering operations: a review. *Rock Mech Rock Eng* 55:629–667. <https://doi.org/10.1007/s00603-021-02687-6>
- Zhang ZX, Yu J, Kou SQ, Lindqvist PA (2001) Effects of high temperatures on dynamic rock fracture. *Int J Rock Mech Min Sci* 34(3):235–242. [https://doi.org/10.1016/S1365-1609\(00\)00071-X](https://doi.org/10.1016/S1365-1609(00)00071-X)

Publisher's Note Springer Nature remains neutral with regard to jurisdictional claims in published maps and institutional affiliations.